The Astrophysical Journal, 560:675–688, 2001 October 20


# *CHANDRA* OBSERVATIONS OF THE X-RAY POINT SOURCE POPULATION IN CENTAURUS A

R. P. Kraft, J. M. Kregenow,[1] W. R. Forman, C. Jones, and S. S. Murray
Harvard/Smithsonian Center for Astrophysics, 60 Garden Street, Cambridge, MA 02138
*Received 2001 February 28; accepted 2001 June 29*

## ABSTRACT

We present results from two *Chandra X-ray Observatory* observations of the X-ray point source population in the nearby radio galaxy Centaurus A (NGC 5128). Using a wavelet decomposition detection algorithm, we detect 246 individual point sources above a limiting luminosity of $\sim 2 \times 10^{36}$ ergs s$^{-1}$, 82 of which are detected in both data sets where the fields of view overlap. Thirty-eight sources were detected in only one observation but were within the field of view of both pointings, implying considerable variability. We identify eight foreground stars in our observations. We also identify nine of the sources with known globular clusters in Centaurus A. All previously observed *ROSAT* sources within our field of view are detected. The number of luminous ($L_x > 10^{37}$ ergs s$^{-1}$) X-ray binaries per unit optical luminosity in Cen A is roughly consistent with that observed for the M31 bulge. There are approximately 50% more X-ray binaries per unit optical luminosity in Centaurus A than in the whole of M31, however. We find considerably fewer luminous X-ray binaries per unit optical luminosity in Cen A than in two other elliptical galaxies, M84 and NGC 4697, recently observed by *Chandra.* This result directly confirms the variance in the X-ray binary population with host galaxy optical luminosity previously inferred from spectral analysis of *ROSAT* and *ASCA* observations of elliptical galaxies.

*Subject headings:* galaxies: active — galaxies: individual (Centaurus A, NGC 5128) — X-rays: galaxies

*On-line material:* machine-readable table

## 1. INTRODUCTION

Centaurus A (NGC 5128, Cen A) is the nearest active galaxy to the Milky Way (at a distance $\sim$3.5 Mpc, $1' \sim 1$ kpc) and has been well studied in all wavelengths from radio to gamma-rays (e.g., for a recent review, see Israel 1998). Cen A exhibits a complex spatial morphology in the radio from scales of milliarcseconds to degrees and is often considered to be the prototypical Fanaroff-Riley class I low-luminosity radio galaxy. Radio observations show a milliarcsecond scale superluminal jet (Tingay et al. 1998) near the active nucleus, a one-sided kiloparsec scale jet extending 6′ NE of the nucleus, and two radio lobes (NE and SW of the nucleus) (Burns, Feigelson, & Schreier 1983). These gradually merge into a more extended, low surface brightness radio source that extends several degrees on the sky. Optically Cen A appears to be an elliptical galaxy crossed by a dark dust lane that lies roughly perpendicular to the radio jet. The dust lane is thought to be the result of a merger with a spiral galaxy (Schminovich et al. 1994). Previous observations in soft X-rays have shown several distinct emission components (Feigelson et al. 1981; Turner et al. 1997). These include a bright nucleus that varied in intensity by 60% over a 15 year time period, a strong X-ray jet perpendicular to the dust lanes and extending 4′ toward the NE radio lobe, diffuse emission from the hot phase of the ISM, and several dozen point sources.

Cen A was observed five times with the *Chandra X-ray Observatory* (*CXO*), three times with the High Resolution Camera (HRC) as part of the Orbital Activation and Checkout phase of the mission, and twice with the Advanced CCD Imaging Spectrometer (ACIS) as part of the HRC program (PI: S. S. Murray). Preliminary results of the HRC observations have been published elsewhere (Kraft et al. 2000; Karovska et al. 2000). The *CXO*'s unprecedented angular resolution coupled with Centaurus A's proximity allows us to make a detailed study of its X-ray emission including knots in the jet, a diffuse emission surrounding the active nucleus, and many individual X-ray point sources that are most likely X-ray binaries (XRB) and perhaps supernova remnants.

In this paper, we present an analysis of the X-ray point source population of Cen A from the two ACIS observations, focusing on an investigation of source properties including their luminosities, spectra, and spatial distribution. We compare our sources with those detected in the *ROSAT* observations (Turner et al. 1997) and investigate possible correlations of the X-ray sources with known Cen A globular clusters, foreground stars, and background galaxies. We examine the light curves and spectra of each individual source and compute a luminosity function, the spectral hardness ratios, and the spatial density distribution for the sources. Prior to *Chandra*, similar detailed studies of the X-ray point source populations have been conducted on a few nearby galaxies such as M31, the Milky Way, and the Magellanic Clouds. Since launch in 1999, *Chandra* has observed a variety of galaxies including M84 (Finoguenov & Jones 2001), NGC 4697 (Sarazin, Irwin, & Bregman 2000), NGC 1553 (Blanton, Sarazin, & Irwin 2001), NGC 1291 (Irwin, Bregman, & Sarazin 2000), M81 (Tennant et al. 2001), M82 (Matsumoto et al. 2001), and NGC 4038/4039 (Fabbiano, Zezas, & Murray 2000). The increased sensitivity of the *CXO* allows detailed investigation of these XRB populations in much more distant galaxies. This study of the population of X-ray point sources in Centaurus A is one of the first such comprehensive surveys for an elliptical galaxy, or a galaxy with an active nucleus.

This paper is organized as follows. Details of the instrumentation, the event list filtering, and the observing log are presented in § 2. The wavelet decomposition source detection algorithm and the source list are presented in § 3. The comparison of our source list with objects detected in other

[1] Department of Physics, Wittenberg University, Springfield, OH 45501.

bands and previous X-ray observations is contained in § 4. This section also includes a discussion of the sensitivity of the observations, the luminosity function, and an analysis of the spectral and temporal properties of the sources. A more detailed discussion of some of the more unusual sources, based on their spectral or temporal properties, is contained in § 5. Section 6 contains a brief summary and conclusion.

## 2. INSTRUMENTATION AND DATA ANALYSIS

The *CXO* consists of four nested paraboloid-hyperboloid confocal, iridium-coated mirrors (the High Resolution Mirror Assembly or HRMA), and two sets of focal plane detectors, the Advanced CCD Imaging Spectrometer (ACIS) and the High-Resolution Camera (HRC). A full description of the *CXO* and its capabilities is given elsewhere (Weisskopf et al. 2000). The observations presented in this paper were made with the ACIS imaging detector (ACIS-I), an array of four frontside illuminated CCDs with a field of view of $\sim 16' \times 16'$. Each pixel on the ACIS-I instrument corresponds to $0''.492 \times 0''.492$ on the sky. The imaging resolution of the HRMA/ACIS-I combination near the telescope axis is limited by the ACIS pixel size to be $\sim 0''.5$. Because of the effects of a large dose of low-energy protons to which the ACIS-I instrument was exposed early in the mission, the energy resolution has been significantly degraded. The temporal resolution is 3.3 s, the time required to read out one frame. Two observations of Centaurus A were made with the ACIS-I (observation IDs: 00316 and 00962) on 1999 December 5 and 2000 May 17, with 35.9 and 36.5 ks exposures, respectively. A more detailed observing log is contained in Table 1. An adaptively smoothed, exposure corrected image in the 1–3 keV bandpass of an $8' \times 8'$ region around the nucleus is shown in Figure 1. Although each data set was analyzed separately, there was considerable overlap in the fields of view of the two observations. The FOV of each of the observations is overlaid onto an optical DSS image in Figure 2. The two observations were made at different roll angles, but the central region of the galaxy was well centered on the ACIS-I3 CCD in both observations. The central region of the galaxy within 7′ of the nucleus was covered in both observations.

The raw events were filtered to include only those with grades 0, 2, 3, 4, and 6. Events occurring at a boundary between output nodes were removed due to uncertainties in reconstruction of the event grade. To maximize source detection, the data were filtered in energy to include only events between 0.4 and 5 keV, since the majority of the events in the 5 to 10 keV range are background, and the response of the ACIS-I instrument drops rapidly below 0.4 keV. All events with PI (invariant pulse-height) equal to 0, 1, or 1024 were removed, as they represent a nonphysical signal. Hot pixels and columns were removed using the standard table provided by the *Chandra* X-ray Center (CXC). Short-term transients due to cosmic rays that create events in the same pixel for three or more consecutive frames that could mimic point sources also were removed (L. P. Van Speybroeck 2000, private communication).

Exposure maps were created for each CCD in the detector array, using the program "mkexpmap" of the *Chandra* Interactive Analysis of Observations (CIAO) software package. These maps correct for three factors that create considerable spatial nonuniformity in the effective area of the instrument. First, the telescope slowly dithers around the target location so that different parts of the detector are exposed for different amounts of time. This is particularly important around the edges of the detector and in the gaps between the ACIS chips. Second, the exposure map accounts for the position-dependent effective area of the telescope, that degrades with off-axis position due to the decreasing reflectivity of the telescope with increasing angle. And third, the decreased charge transfer efficiency of ACIS creates a spatially dependent sensitivity variation. We created the maps at 1.5 keV where the source spectra generally peak. This assumption of monochromaticity introduces little systematic error.

Individual point sources were detected using the CIAO program "wavdetect" that uses a wavelet decomposition algorithm. We chose a wavelet detection algorithm because of the complex, nonuniform emission from the hot ISM of the galaxy. It is necessary to make a local determination of the background for each source to accurately compute its significance and flux. A local background is computed with the wavelet decomposition. In addition, the point spread function (PSF) is considerably broadened for sources off the telescope axis. Again, the wavelet algorithm accounts for the PSF variations by searching for sources on different spatial scales. The source list generated by wavdetect was visually compared with the unsmoothed image to confirm that every source it detected was indeed a source. We likewise inspected the image to ensure that all sources visible by eye were detected. It was not our goal to test the efficiency of the wavdetect software, but simply to ensure that no obvious sources were missed. In our detailed analysis of the point source population below, we have chosen a very conservative (minimum 4 $\sigma$ flux measurement) flux limit above which we are confident that no source was missed.

For the purposes of this study which focuses on the X-ray point source population, we omitted sources located within the X-ray jet. This was done by visually excluding any source that lay within the enhanced diffuse emission along the jet. It is likely that some of the knots in the jet are actually XRBs, but the low count rate from most of the knots combined with the enhanced diffuse emission from the jet makes the identification of pointlike sources difficult.

TABLE 1

OBSERVATION LOG OF *Chandra*/ACIS-I OBSERVATIONS OF CENTAURUS A

| Obs. ID | Date | Exp. Time (ks) | R.A. | Decl. | *Y* Offset | *Z* Offset | SIM Z |
|---|---|---|---|---|---|---|---|
| 00316...... | 1999 Dec 05 | 35.9 | 13 25 27.61 | −43 01 08.9 | 3′ | 3′ | 0.0 |
| 00962...... | 2000 May 17 | 36.5 | 13 25 27.61 | −43 01 08.9 | −3′ | 0′ | −5.88 mm |

NOTES.—The columns in the table are the observation ID, the date of observation, the length of the observation, the R.A. and decl. of the center of the galaxy, the pointing offsets, and the SIM translation. Units of right ascension are hours, minutes, and seconds, and units of declination are degrees, arcminutes, and arcseconds.

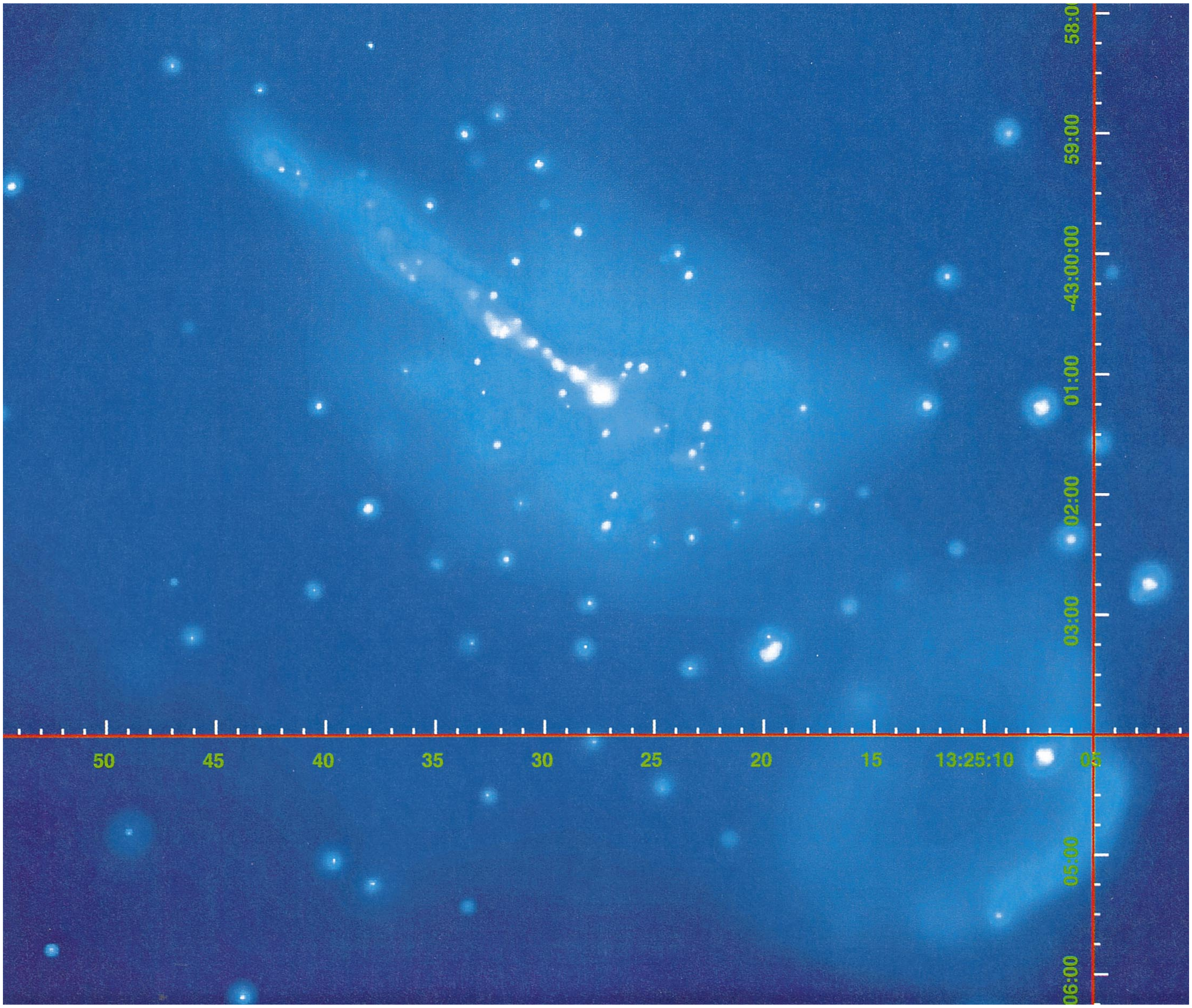


FIG. 1.—Adaptively smoothed, exposure corrected, co-added image in the 1–3 keV bandpass of Cen A. North is up and east is to the left. Note the bright nucleus at the center, the jet extending to the NE, the diffuse emission around the galaxy, and the many point sources.

The X-ray flux from the nucleus is so large that there are a considerable number of "out of time" events that are incident on the detector during frame transfer. These events manifest themselves as a streak along the detector through the nucleus. A 9″ wide region in each observation along this frame transfer streak also was excluded from our analysis.

The absolute alignment of the aspect system on *Chandra* is generally good to 1″–2″ (Aldcroft et al. 2000). We have independently verified the absolute alignment on the sky by comparing our X-ray source list with the USNO-A2.0 stellar catalog (Monet 1998). We found six X-ray sources in the two observations that correspond to stars in the USNO catalog and made a small adjustment ($\sim 1''$) in the coordinates to align the two data sets on the sky. All six sources are near the edge of the field of view where the uncertainty in the source position is largest, but from this comparison, we estimate that the error (rms) on our absolute position is $\sim 0''.5$. We note that using our best coordinates, the radio and X-ray positions of knot A1 of the jet are coincident to $\sim 0''.5$.

## 3. POINT SOURCE DISTRIBUTION AND LUMINOSITY FUNCTION

A total of 246 sources were detected in the two ACIS-I observations, 82 of which were detected in both observations. The complete list of sources from both observations is contained in Table 2. The positions of the sources are overplotted onto an optical DSS *J*-band image of Cen A in Figure 3. The source count rates were converted to a source luminosity assuming a distance of 3.5 Mpc to Cen A, and 5 keV bremsstrahlung spectrum with Galactic absorption ($7 \times 10^{20}$ cm$^{-2}$). The conversion between count rate in the 0.4–5 keV band and absorbed flux in the 0.4–10 keV band, obtained from the HEASARC PIMMS, is $10^{-3}$ counts s$^{-1}$ = $9.8 \times 10^{-15}$ ergs cm$^{-2}$ s$^{-1}$. The unabsorbed flux in the 0.4–10 keV energy band is 9% larger. The faintest source in our list has 5 counts, which corresponds to a

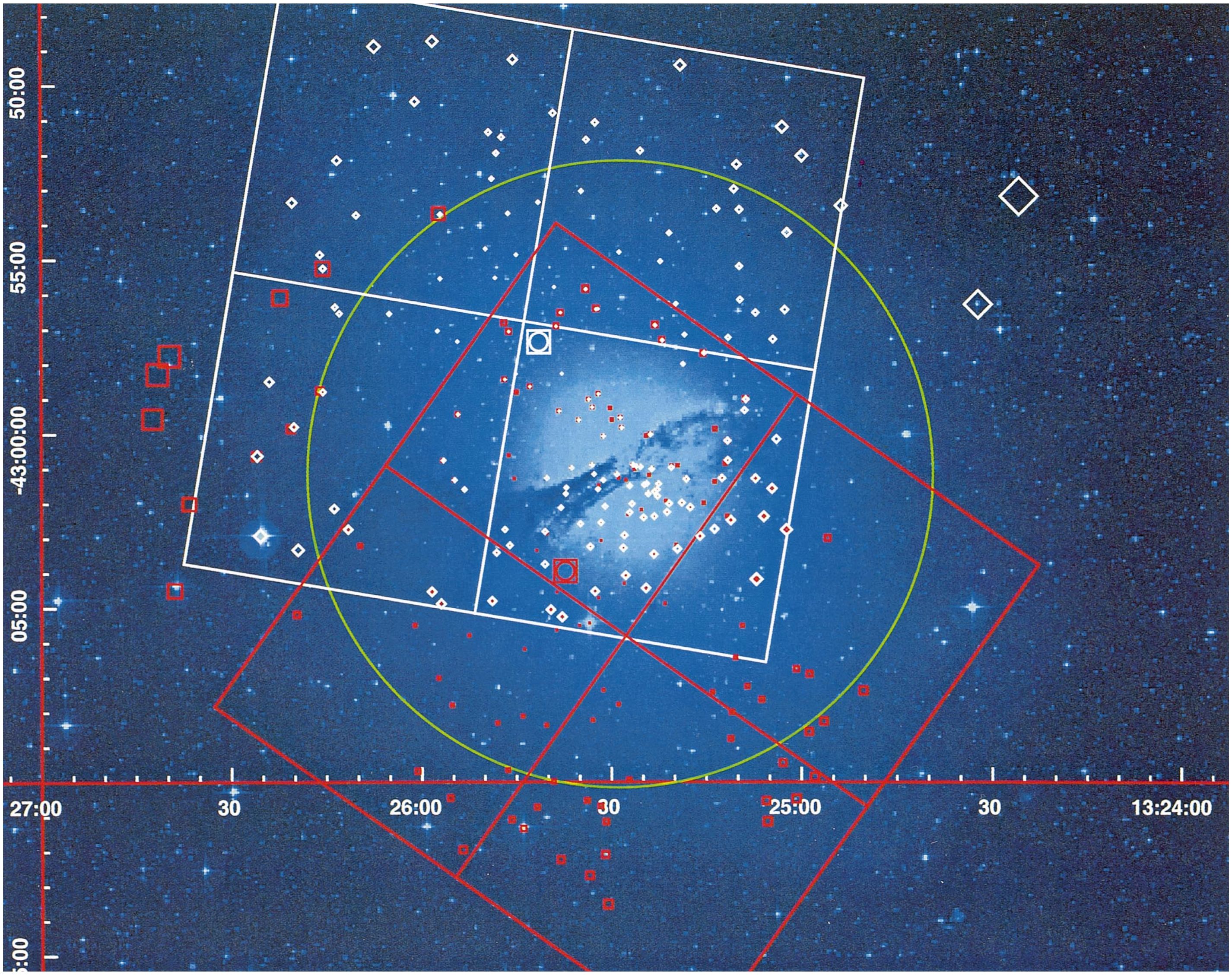


FIG. 2.—FOV of the two *Chandra* observations (OBSID 00316—*white*, OBSID 00962—*red*) overlaid onto an optical DSS image (*J* band) of Cen A. Both observations were aligned so that the central region of Cen A was well centered on the ACIS I3 CCD. The detected sources from each of the observations have also been overlaid (with the same color scheme) as boxes. The size of the box is proportional to the PSF at that location. The nominal pointing position for each observation is shown as the box with an inscribed circle. Note that several sources appear to be located off the boundaries of the detector. These are sources that were detected on the ACIS-S chips, the boundaries of which are not shown. The green circle delineates the 9′ diameter region used in the comparison between Cen A and other galaxies described below.

limiting luminosity of $\sim 2.2 \times 10^{36}$ ergs s$^{-1}$ at the center of the field of view.

A plot of the surface density of sources (number per square arcminute) versus distance from the nucleus of Cen A is shown in Figure 4. The surface density plot is peaked at the center as one would expect if the majority of sources are related to the galaxy and not foreground or background objects. The surface density plot flattens beyond about 9′ from the nucleus, indicating that most of the sources beyond this distance are either foreground or background objects and are therefore unrelated to Cen A. This result is consistent with the optical ($D_{25} = 14' \times 18'$) size of the galaxy (Israel 1998). The surface density of sources beyond 9′ is roughly consistent with the expected surface density ($\sim 0.25$ sources per arcmin$^2$) of background AGNs based on *Chandra* observations of the *Chandra* Deep Field South (Giacconi et al. 2000). There is a significant clustering of sources in a region $\sim 1\rlap{.}'5$ SW of the nucleus. There is an enhancement of diffuse emission in this region as well. Several of these sources lie in a line running from the jet through nucleus in the opposite direction from the jet, suggestive of a possible counterjet. Since none of these point sources are coincident with any of the knots of radio emission seen in the SW radio lobe (Clarke, Burns, & Norman 1992), we consider it unlikely that these sources are related to any collimated outflow from the nucleus (Kraft et al. 2001). It is possible that the large number of X-ray point sources in this region is related to enhanced star formation.

### 3.1. *Sensitivity and Luminosity Function*

The log *N*–log *S* curve of all the detected sources for each observation is plotted in Figure 5. Also shown is an estimate of the number of background AGNs as a function of flux based on the recent *Chandra* observations of the *Chandra* Deep Field South (Giacconi et al. 2000). The differential luminosity function is shown in Figure 6. The sensitivity of the observations varies across the field of view due

TABLE 2

Summary of X-Ray Point Sources Detected in Cen A Observation

| R.A. (1) | Decl. (2) | 316 Lum (3) | 962 Lum (4) | Notes (5) |
|---|---|---|---|---|
| 13 24 26.45 | −42 53 09.21 | 1.56E+37 | | |
| 13 24 32.82 | −42 56 15.29 | 2.70E+38 | | P5; fgs |
| 13 24 50.56 | −43 07 21.22 | | 9.58E+36 | |
| 13 24 54.27 | −42 53 26.20 | 1.53E+37 | | |
| 13 24 56.26 | −43 02 58.25 | | 5.25E+36 | |
| 13 24 56.74 | −43 08 14.17 | | 6.54E+37 | |
| 13 24 58.14 | −43 09 50.01 | | 3.35E+37 | |
| 13 24 59.05 | −43 06 52.74 | | 3.89E+36 | |
| 13 24 59.05 | −43 08 32.21 | | 5.32E+36 | |
| 13 25 00.44 | −42 52 00.13 | 5.66E+37 | | P2 |
| 13 25 01.00 | −43 10 28.23 | | 1.33E+37 | fgs |
| 13 25 01.08 | −43 06 44.20 | | 4.63E+37 | fgs |
| 13 25 02.72 | −43 02 43.79 | 1.51E+38 | 1.73E+38 | P14 |
| 13 25 02.72 | −42 54 12.50 | 3.26E+37 | | fgs |
| 13 25 03.04 | −42 56 25.09 | 1.37E+37 | | GC |
| 13 25 03.15 | −43 09 25.88 | | 1.37E+37 | |
| 13 25 03.52 | −42 51 10.56 | 6.70E+36 | | |
| 13 25 04.32 | −43 00 07.95 | 9.69E+36 | <3.57E+36 | ltv |
| 13 25 04.90 | −42 57 15.88 | 4.48E+36 | | |
| 13 25 05.01 | −43 01 33.41 | 2.43E+37 | 3.19E+37 | |
| 13 25 05.54 | −43 11 07.20 | | 3.63E+37 | stv |
| 13 25 05.75 | −43 10 31.51 | | 1.14E+37 | GC |
| 13 25 06.31 | −43 02 21.09 | 1.19E+38 | 6.68E+37 | P11; ltv |
| 13 25 06.56 | −43 07 36.77 | | 5.40E+36 | |
| 13 25 07.45 | −43 04 09.53 | 4.24E+38 | 1.05E+39 | P18; stv; ltv |
| 13 25 07.64 | −43 01 15.49 | 2.59E+38 | 2.39E+38 | |
| 13 25 07.65 | −42 56 30.23 | 2.34E+37 | | |
| 13 25 08.81 | −43 07 14.29 | | 2.37E+36 | |
| 13 25 09.20 | −42 58 59.64 | 5.05E+37 | 4.12E+37 | |
| 13 25 09.33 | −42 59 18.40 | 4.44E+36 | <6.77E+36 | |
| 13 25 09.63 | −43 05 29.56 | | 3.01E+37 | |
| 13 25 10.09 | −42 56 07.89 | 1.27E+37 | | |
| 13 25 10.21 | −42 55 10.46 | 2.51E+37 | | |
| 13 25 10.22 | −42 53 33.21 | 3.72E+37 | | |
| 13 25 10.66 | −42 52 15.18 | 4.91E+36 | | |
| 13 25 10.70 | −43 06 24.65 | <2.62E+36 | 4.69E+37 | ltv |
| 13 25 11.06 | −42 52 57.52 | 5.22E+36 | | |
| 13 25 11.24 | −43 07 58.19 | | 2.32E+36 | |
| 13 25 11.39 | −43 08 44.31 | | 1.72E+37 | SSS |
| 13 25 11.52 | −43 02 27.09 | 1.24E+37 | 1.42E+37 | |
| 13 25 11.93 | −42 57 12.82 | 8.05E+36 | <8.36E+36 | |
| 13 25 11.99 | −43 00 44.63 | 3.61E+37 | 2.93E+37 | |
| 13 25 12.00 | −43 00 10.79 | 3.28E+37 | 3.14E+37 | |
| 13 25 12.04 | −43 02 20.47 | <3.84E+36 | 9.39E+36 | ltv, SSS |
| 13 25 12.36 | −43 00 49.55 | <4.30E+36 | 5.62E+36 | ltv |
| 13 25 12.89 | −43 01 14.69 | 7.21E+37 | 6.12E+37 | |
| 13 25 13.78 | −42 53 31.48 | 4.23E+37 | | |
| 13 25 14.03 | −42 59 50.33 | <5.85E+36 | 4.40E+36 | |
| 13 25 14.03 | −43 02 42.90 | 6.02E+36 | <1.51E+36 | ltv |
| 13 25 14.04 | −43 01 21.22 | <4.26E+36 | 5.65E+36 | ltv |
| 13 25 14.29 | −43 07 24.00 | | 2.57E+37 | |
| 13 25 15.82 | −42 57 39.66 | 1.26E+37 | 8.83E+36 | |
| 13 25 15.79 | −43 01 58.10 | <4.47E+36 | 7.05E+36 | ltv |
| 13 25 16.40 | −43 02 55.25 | 2.99E+37 | 1.31E+37 | |
| 13 25 17.87 | −43 02 05.09 | 3.45E+37 | 2.36E+37 | |
| 13 25 18.50 | −43 01 16.34 | 3.36E+37 | 3.47E+37 | |
| 13 25 18.80 | −42 57 08.08 | 9.23E+36 | <4.41E+36 | ltv |
| 13 25 19.05 | −42 57 58.59 | 2.66E+36 | <4.04E+36 | |
| 13 25 19.19 | −43 01 57.35 | 1.48E+37 | 1.56E+37 | |
| 13 25 19.54 | −42 49 24.41 | 3.73E+37 | | |
| 13 25 19.87 | −43 03 17.14 | 9.03E+38 | <1.69E+36 | ltv |
| 13 25 19.90 | −43 00 53.28 | | 6.73E+36 | |
| 13 25 20.09 | −43 03 10.10 | | 2.49E+37 | |
| 13 25 20.19 | −42 56 15.26 | 8.15E+36 | <5.61E+36 | ltv |
| 13 25 20.86 | −43 00 53.65 | | 1.11E+37 | |
| 13 25 20.87 | −43 00 56.96 | 5.43E+36 | | |
| 13 25 21.27 | −43 01 58.80 | 1.77E+37 | 1.09E+37 | |
| 13 25 21.24 | −42 54 13.35 | 3.98E+37 | | |
| 13 25 21.56 | −43 02 13.73 | 1.17E+37 | 1.29E+37 | |
| 13 25 21.75 | −43 01 54.15 | <6.27E+36 | 6.65E+36 | ltv |
| 13 25 21.84 | −43 04 51.34 | <4.72E+36 | 5.12E+36 | ltv |
| 13 25 22.36 | −42 57 17.09 | 6.92E+37 | 5.74E+37 | P8 |
| 13 25 22.65 | −42 55 01.95 | 3.65E+37 | | |
| 13 25 22.88 | −43 01 24.95 | 1.40E+38 | 7.48E+37 | ltv |
| 13 25 23.06 | −43 01 45.81 | 2.20E+37 | 1.79E+37 | |
| 13 25 23.10 | −43 01 34.39 | 1.99E+37 | 1.85E+37 | |
| 13 25 23.49 | −42 56 51.54 | 1.76E+37 | 1.70E+37 | |
| 13 25 23.54 | −43 01 38.45 | 4.01E+37 | 4.74E+37 | |
| 13 25 23.57 | −43 02 20.72 | 2.35E+37 | 2.77E+37 | |
| 13 25 23.62 | −43 03 26.09 | 2.99E+37 | 3.00E+37 | |
| 13 25 23.66 | −43 00 09.67 | 1.05E+38 | | |
| 13 25 23.96 | −43 00 59.39 | 2.16E+37 | 2.96E+37 | |
| 13 25 24.20 | −42 59 59.41 | 4.88E+37 | 4.52E+37 | |
| 13 25 24.39 | −43 01 09.96 | | 8.34E+36 | |
| 13 25 24.51 | −43 01 41.88 | 9.73E+36 | 9.35E+36 | |
| 13 25 24.76 | −43 01 24.77 | 1.87E+37 | 1.52E+37 | |
| 13 25 24.88 | −43 04 25.24 | 1.69E+37 | 1.59E+37 | |
| 13 25 24.87 | −43 00 02.05 | <3.18E+36 | 1.02E+37 | ltv |
| 13 25 25.15 | −43 01 26.81 | 2.43E+37 | 2.30E+37 | |
| 13 25 25.26 | −43 02 23.01 | 1.40E+37 | 1.76E+37 | |
| 13 25 25.59 | −43 02 09.68 | <5.91E+36 | 1.16E+37 | ltv |
| 13 25 25.76 | −43 00 55.98 | 6.83E+37 | 1.34E+38 | ltv |
| 13 25 25.83 | −42 51 51.74 | 1.21E+37 | | |
| 13 25 26.43 | −43 00 54.40 | 1.02E+38 | 1.14E+38 | |
| 13 25 26.71 | −43 00 59.56 | | 2.72E+37 | |
| 13 25 26.96 | −43 00 52.57 | 1.40E+37 | 1.18E+37 | |
| 13 25 27.10 | −43 01 59.34 | 4.49E+37 | 5.57E+37 | |
| 13 25 27.49 | −43 01 28.43 | 3.86E+37 | 4.96E+37 | GC |
| 13 25 27.44 | −43 09 55.06 | | 1.75E+37 | |
| 13 25 27.45 | −43 02 14.10 | 1.33E+38 | 6.75E+37 | ltv |
| 13 25 27.71 | −43 02 17.80 | <6.39E+36 | 1.11E+37 | ltv |
| 13 25 28.04 | −43 04 02.81 | 1.54E+37 | 1.60E+37 | |
| 13 25 28.06 | −43 01 18.51 | | 1.19E+37 | |
| 13 25 28.25 | −43 02 53.52 | 2.51E+37 | 2.68E+37 | |
| 13 25 28.32 | −43 04 16.56 | <4.41E+36 | 5.57E+36 | ltv |
| 13 25 28.45 | −43 03 15.47 | 2.08E+37 | 2.07E+37 | |
| 13 25 28.75 | −42 59 48.23 | 9.14E+37 | 7.72E+37 | |
| 13 25 28.96 | −42 59 30.83 | 3.81E+36 | 5.06E+36 | |
| 13 25 29.14 | −42 54 46.35 | 3.74E+36 | | |
| 13 25 29.15 | −43 07 44.94 | | 7.05E+36 | |
| 13 25 29.23 | −43 01 14.78 | | 1.04E+37 | |
| 13 25 29.45 | −43 01 08.36 | 3.86E+37 | 2.61E+37 | |
| 13 25 30.29 | −42 59 34.64 | <1.58E+36 | 8.88E+36 | GC; ltv |
| 13 25 30.57 | −42 59 14.57 | <1.23E+36 | 1.94E+38 | ltv |
| 13 25 30.75 | −43 13 30.32 | | 7.98E+36 | |
| 13 25 31.11 | −43 11 07.53 | | 7.62E+37 | |
| 13 25 31.20 | −43 12 04.37 | | 5.39E+36 | |
| 13 25 31.34 | −43 02 03.98 | 1.88E+37 | <1.54E+36 | ltv |
| 13 25 31.57 | −43 07 20.68 | | 5.31E+36 | |
| 13 25 31.61 | −43 00 03.06 | 7.62E+37 | 6.45E+37 | GC |
| 13 25 31.63 | −43 01 18.90 | 5.47E+36 | | |
| 13 25 31.93 | −43 10 40.39 | | 4.36E+36 | |
| 13 25 31.97 | −43 03 02.61 | <3.94E+36 | 2.70E+36 | |
| 13 25 32.02 | −43 02 31.57 | 4.28E+37 | 4.41E+37 | |
| 13 25 32.35 | −43 01 27.19 | | 3.69E+36 | |
| 13 25 32.38 | −43 04 41.57 | <4.85E+36 | 3.48E+36 | |
| 13 25 32.44 | −42 58 49.98 | 1.93E+37 | 1.75E+37 | GC |
| 13 25 32.48 | −43 01 34.14 | 5.58E+37 | 5.48E+37 | |
| 13 25 32.50 | −42 56 23.90 | 3.21E+36 | | |
| 13 25 32.80 | −42 56 23.83 | 4.82E+36 | 8.35E+36 | |

TABLE 2—*Continued*

| R.A. (1) | Decl. (2) | 316 Lum (3) | 962 Lum (4) | Notes (5) |
|---|---|---|---|---|
| 13 25 32.92 | −43 04 29.81 | 8.44E+36 | 1.19E+37 | |
| 13 25 32.96 | −42 51 03.15 | 7.36E+37 | | |
| 13 25 33.09 | −43 01 08.21 | 1.98E+37 | 1.93E+37 | |
| 13 25 33.24 | −43 08 12.12 | | 8.47E+36 | |
| 13 25 33.38 | −42 59 13.02 | 4.27E+36 | 6.93E+36 | |
| 13 25 33.38 | −43 00 52.73 | 2.72E+37 | 3.98E+37 | |
| 13 25 33.67 | −43 12 40.32 | | 4.81E+36 | |
| 13 25 33.68 | −43 03 13.32 | 1.44E+37 | 1.39E+37 | |
| 13 25 33.78 | −43 05 25.24 | <3.98E+36 | 8.41E+36 | fgs; ltv |
| 13 25 33.95 | −42 58 59.53 | 3.89E+37 | 4.46E+37 | P9; GC |
| 13 25 34.11 | −43 10 31.08 | | 1.08E+37 | |
| 13 25 34.34 | −42 51 32.64 | 2.78E+36 | | |
| 13 25 34.43 | −42 55 49.61 | 7.33E+36 | 5.48E+36 | |
| 13 25 35.13 | −42 53 01.28 | 9.44E+37 | | |
| 13 25 35.23 | −43 02 33.56 | 8.32E+36 | 5.55E+36 | |
| 13 25 35.35 | −43 05 29.37 | <3.86E+36 | 5.18E+36 | ltv |
| 13 25 35.52 | −42 59 35.16 | 4.66E+37 | 3.90E+37 | |
| 13 25 36.64 | −43 00 57.53 | 7.73E+36 | 2.70E+37 | ltv |
| 13 25 37.46 | −43 01 31.43 | 5.10E+36 | 5.71E+36 | |
| 13 25 37.54 | −43 01 42.41 | 3.31E+36 | <1.83E+36 | ltv |
| 13 25 38.10 | −43 05 14.06 | 1.50E+37 | 1.77E+37 | |
| 13 25 38.18 | −42 58 15.26 | 4.22E+37 | <2.79E+36 | ltv |
| 13 25 38.24 | −43 12 13.04 | | 2.91E+37 | |
| 13 25 38.33 | −43 02 05.81 | 1.68E+38 | 1.59E+38 | |
| 13 25 38.43 | −42 56 30.48 | 7.19E+36 | 7.29E+36 | |
| 13 25 38.62 | −42 59 19.56 | 8.45E+36 | 8.14E+36 | GC |
| 13 25 38.92 | −43 04 31.79 | <5.90E+36 | 3.95E+36 | |
| 13 25 38.96 | −43 05 37.25 | <1.19E+37 | 2.36E+36 | |
| 13 25 39.10 | −42 56 53.52 | 4.46E+37 | 2.40E+37 | |
| 13 25 39.39 | −42 55 46.34 | 3.23E+36 | <1.22E+36 | ltv |
| 13 25 39.40 | −43 09 58.05 | | 6.74E+36 | |
| 13 25 39.61 | −42 50 46.85 | 6.32E+36 | | |
| 13 25 39.89 | −43 05 02.04 | 1.41E+37 | 2.02E+37 | |
| 13 25 40.51 | −43 02 51.30 | <3.51E+36 | 2.74E+36 | |
| 13 25 40.57 | −43 01 15.05 | 3.61E+37 | 4.70E+37 | |
| 13 25 40.57 | −43 08 20.89 | | 3.33E+36 | |
| 13 25 40.82 | −43 03 43.64 | 2.76E+36 | | |
| 13 25 40.84 | −43 02 46.85 | 1.11E+37 | 1.64E+37 | |
| 13 25 41.93 | −42 53 20.47 | 2.36E+36 | | fgs |
| 13 25 42.03 | −43 10 42.43 | | 2.34E+38 | P25 |
| 13 25 42.13 | −43 03 19.73 | <4.23E+36 | 2.37E+36 | |
| 13 25 43.25 | −42 58 37.26 | 2.41E+37 | 1.76E+37 | |
| 13 25 44.04 | −43 06 10.23 | | 5.00E+37 | |
| 13 25 44.19 | −43 11 19.34 | | 3.01E+37 | fgs |
| 13 25 44.27 | −43 08 05.35 | | 5.75E+37 | |
| 13 25 45.38 | −42 58 47.44 | | 2.84E+36 | |
| 13 25 45.38 | −42 54 50.79 | 2.01E+37 | | |
| 13 25 45.45 | −42 58 15.59 | 9.96E+36 | <2.43E+36 | ltv |
| 13 25 45.70 | −43 01 15.90 | <2.16E+36 | 3.58E+36 | ltv |
| 13 25 45.96 | −42 49 14.66 | 1.00E+37 | | |
| 13 25 46.03 | −43 11 03.95 | | 1.41E+38 | H17 |
| 13 25 46.38 | −43 03 10.61 | 1.79E+37 | 1.87E+37 | |
| 13 25 46.57 | −43 00 35.99 | | 7.03E+36 | |
| 13 25 46.59 | −42 57 02.69 | 3.11E+37 | 3.37E+37 | GC |
| 13 25 46.61 | −43 09 38.22 | | 3.32E+37 | |
| 13 25 46.68 | −42 53 39.96 | 2.06E+37 | | |
| 13 25 47.19 | −43 02 43.45 | 6.79E+36 | 9.93E+36 | |
| 13 25 47.24 | −42 58 25.13 | 1.52E+37 | 1.41E+37 | |
| 13 25 47.34 | −42 56 47.40 | <1.08E+37 | 7.78E+36 | |
| 13 25 47.74 | −42 51 28.31 | 2.32E+37 | | |
| 13 25 48.26 | −43 08 17.24 | | 1.04E+37 | |
| 13 25 48.53 | −43 03 23.19 | 7.50E+36 | 3.99E+36 | |
| 13 25 48.56 | −42 51 55.83 | 6.65E+36 | | |
| 13 25 48.72 | −42 55 30.52 | 1.32E+37 | | |
| 13 25 49.22 | −43 04 47.53 | 5.57E+36 | 9.43E+36 | |
| 13 25 49.27 | −42 52 39.96 | 1.72E+38 | | P4 |
| 13 25 49.78 | −42 51 19.77 | 3.35E+36 | | |
| 13 25 50.24 | −42 54 40.57 | 2.87E+36 | | |
| 13 25 52.79 | −43 05 46.36 | | 1.79E+37 | |
| 13 25 53.55 | −43 01 34.63 | 2.39E+36 | <1.16E+36 | ltv |
| 13 25 53.76 | −43 11 55.73 | | 4.44E+37 | |
| 13 25 54.59 | −42 59 25.26 | 8.74E+37 | 8.47E+37 | P10 |
| 13 25 54.66 | −42 57 19.79 | 6.93E+36 | | |
| 13 25 55.13 | −43 01 18.39 | 7.51E+36 | 6.30E+36 | |
| 13 25 55.44 | −43 07 46.12 | | 5.67E+36 | fgs |
| 13 25 55.74 | −43 10 26.33 | | 3.29E+36 | |
| 13 25 56.91 | −43 00 44.65 | 1.89E+37 | 1.93E+37 | |
| 13 25 57.19 | −43 04 51.76 | 6.30E+36 | | |
| 13 25 57.40 | −42 53 41.49 | 1.74E+37 | | |
| 13 25 57.40 | −42 55 31.76 | 8.25E+36 | | |
| 13 25 57.40 | −43 04 50.05 | | 1.05E+37 | |
| 13 25 57.62 | −43 06 59.62 | | 8.69E+36 | |
| 13 25 57.63 | −42 53 40.27 | | 1.22E+37 | |
| 13 25 57.80 | −42 57 01.60 | 3.22E+37 | | |
| 13 25 58.62 | −42 48 43.04 | 1.07E+37 | | |
| 13 25 58.73 | −43 04 30.72 | 1.73E+38 | 2.93E+38 | H14; ltv |
| 13 26 00.88 | −43 09 40.12 | | 3.07E+37 | |
| 13 26 01.35 | −43 05 28.42 | | 3.78E+38 | H15; P21 |
| 13 26 01.38 | −42 50 27.02 | 2.76E+37 | | |
| 13 26 05.39 | −42 56 32.22 | 5.06E+37 | | |
| 13 26 07.77 | −42 48 52.04 | 1.25E+37 | | |
| 13 26 10.00 | −43 03 11.40 | | 2.83E+36 | |
| 13 26 10.58 | −42 53 42.78 | 1.72E+37 | | |
| 13 26 11.91 | −43 02 43.08 | 5.82E+37 | 5.02E+37 | |
| 13 26 13.25 | −42 56 31.44 | 5.59E+36 | | |
| 13 26 13.60 | −42 52 08.33 | 1.51E+37 | | |
| 13 26 13.93 | −42 56 20.66 | 4.57E+36 | | |
| 13 26 14.05 | −43 02 07.67 | 1.90E+37 | | |
| 13 26 15.83 | −42 55 14.15 | 8.18E+37 | 1.42E+38 | ltv |
| 13 26 15.85 | −42 58 46.50 | 8.58E+37 | | |
| 13 26 16.27 | −42 54 50.62 | 4.44E+36 | | |
| 13 26 16.33 | −42 58 44.41 | | 8.40E+36 | |
| 13 26 19.74 | −43 03 18.62 | 1.89E+37 | | |
| 13 26 19.95 | −43 05 10.14 | | 4.21E+36 | |
| 13 26 20.38 | −42 59 46.67 | 1.75E+37 | | |
| 13 26 20.65 | −42 53 20.78 | 6.43E+36 | | |
| 13 26 20.87 | −42 59 49.97 | | 3.40E+37 | |
| 13 26 22.55 | −42 56 04.76 | | 9.97E+36 | |
| 13 26 24.25 | −42 58 28.88 | 3.01E+36 | | |
| 13 26 25.67 | −43 02 54.34 | 7.18E+37 | | P16 |
| 13 26 26.21 | −43 00 37.08 | 1.09E+37 | 1.79E+37 | |
| 13 26 36.87 | −43 01 59.59 | | 1.37E+37 | |
| 13 26 39.17 | −43 04 28.88 | | 9.78E+36 | |
| 13 26 39.96 | −42 57 44.50 | | 2.38E+37 | |
| 13 26 41.84 | −42 58 16.14 | | 3.11E+37 | |
| 13 26 42.63 | −42 59 32.97 | | 2.86E+37 | |

NOTES.—Columns in this table are the R.A., decl., Luminosity in the 0.4–10 keV band in each observation, and "Notes." Units of right ascension are hours, minutes, and seconds, and units of declination are degrees, arcminutes, and arcseconds. Sources detected in both observations have two luminosities listed. If a source was seen in only one observation but was within the FOV of the other, an upper limit to the luminosity based on a 3 $\sigma$ fluctuation in the background is listed in the other column and preceded by a less-than symbol (<). The last column contains identifications we have made of our sources with foreground stars (fgs) from the USNO A2.0 catalog, globular clusters (GC) (Harris et al. 1984; Minitti et al. 1996), X-ray sources previously observed by the *ROSAT* PSPC detector ("P#") or the HRI detector ("H#") (Turner et al. 1997), or super-soft sources (SSS). We have also labeled whether a source is variable within one of the observations (stv—short-term variable), or between the two observations (ltv—long-term variable). See text for a complete discussion of criteria for variability. Table 2 is also available in machine-readable form in the electronic edition of the *Astrophysical Journal.*

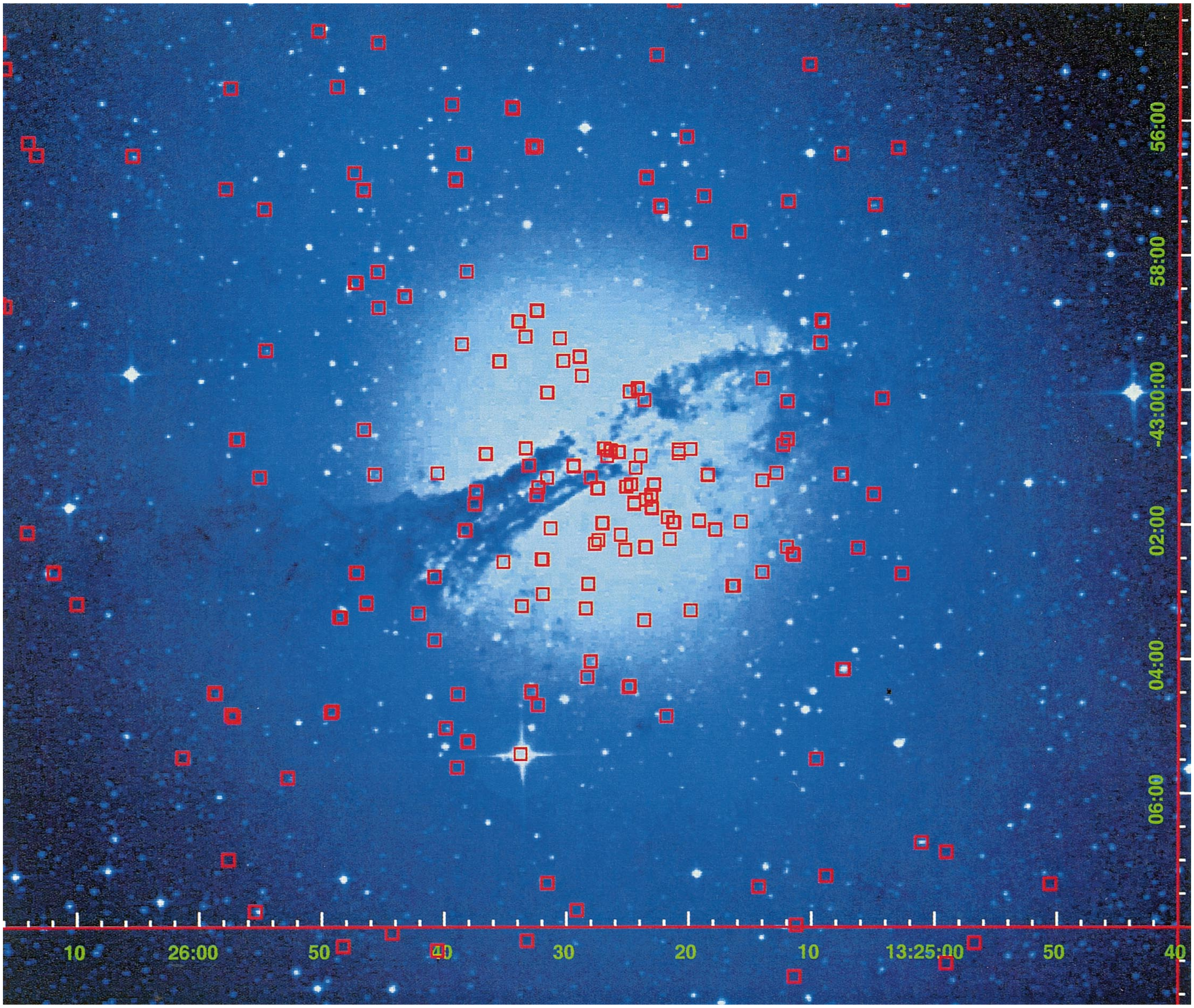


FIG. 3.—Position of X-ray point sources overlaid onto a DSS image ($J$ band) of Cen A

to the telescope vignetting, variations in the PSF across the field of view, and the complex spatial morphology of the diffuse emission from the galaxy. We have made a conservative estimate of the sensitivity where our source detection would be complete by using the measured background and the telescope PSF at the edge of the field of view and requiring a 4 $\sigma$ measurement of the count rate. This value is shown in Figure 5 as the dashed vertical line. The results of a more detailed computation showing the fraction of the field of view having a given sensitivity level (again requiring a 4 $\sigma$ measurement of the source counts) is shown in Figure 7. We used a wavelet decomposition to create a background map from the image with all point sources removed. The sensitivity was then computed using this background map and the telescope vignetting function. In these relatively short ($\sim$35 ks) observations, the sensitivity is limited by the source luminosity, not the background, over most of the field of view.

Our source list was compared with the X-ray sources found by the *ROSAT* observatory (Turner et al. 1997). We detected all of the *ROSAT* sources that were within our field of view, assuming a positional uncertainty of 5″ for the HRI sources and 20″ for the PSPC sources. We also compared our source list with globular cluster lists of Cen A (Harris et al. 1992; Minitti et al. 1996) and find nine of the sources to be coincident within 1″.5 ($\sim$25 pc) with known globular clusters. As stated above, six of our sources are coincident with foreground stars in the USNO-A2.0 stellar catalog. Two additional sources have been identified with foreground objects as described below. The coincidence between our sources and either a globular cluster, a *ROSAT* source, or a foreground star has been listed in Table 2 (col. [5]).

## 4. COMPARISON WITH OTHER GALAXIES

Observations and detailed studies of the X-ray point source populations of galaxies other than the Milky Way have been made in only a few instances. The presence of a large population of XRBs in elliptical galaxies has been inferred from spectral analysis of *Einstein*, *ASCA*, and

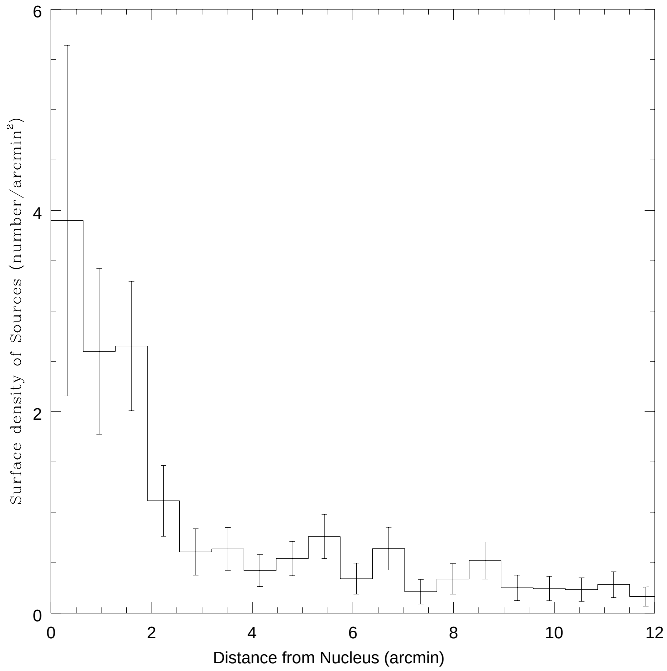


FIG. 4.—Surface density of sources vs. distance from the Cen A nucleus in the first ACIS (OBSID 00316) observation. The radial surface density profile of the second ACIS observation is similar.

*ROSAT* observations (Trinchieri & Fabbiano 1985; Fabbiano, Kim, & Trinchieri 1994; Matsumoto et al. 1997; Irwin & Sarazin 1998; Trinchieri et al. 2000) but never directly observed. This conclusion was reinforced by the statistical analysis of the *Einstein* E and S0 sample

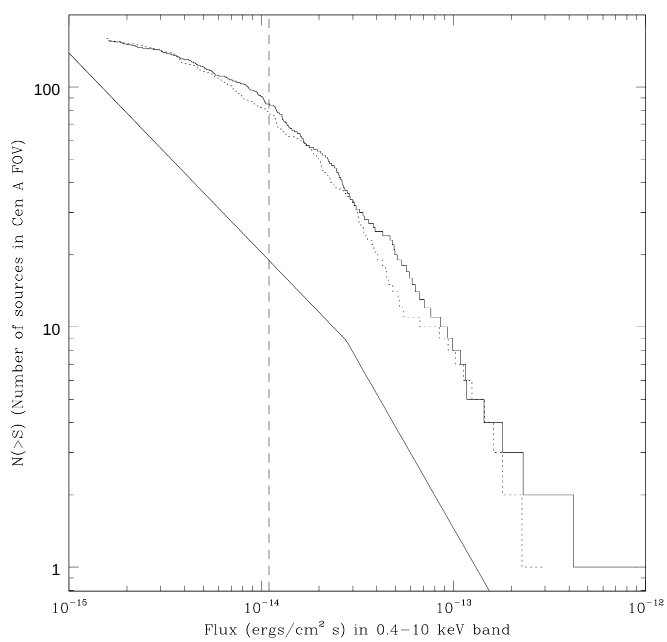


FIG. 5.—log (*N*)–log (*S*) curve of the point sources in each of the observations of Centaurus A in the 0.4–10 keV bandpass. The solid histogram is the first observation (OBSID 00316), and the dashed histogram is the second (OBSID 00962). The solid line is the log (*N*)–log (*S*) relationship for background AGNs based on *Chandra* observations of the *Chandra* Deep Field South (Giacconi et al. 2000). The dashed vertical line is a conservative estimate of the flux at which our sample is complete and unbiased. See text for full details.

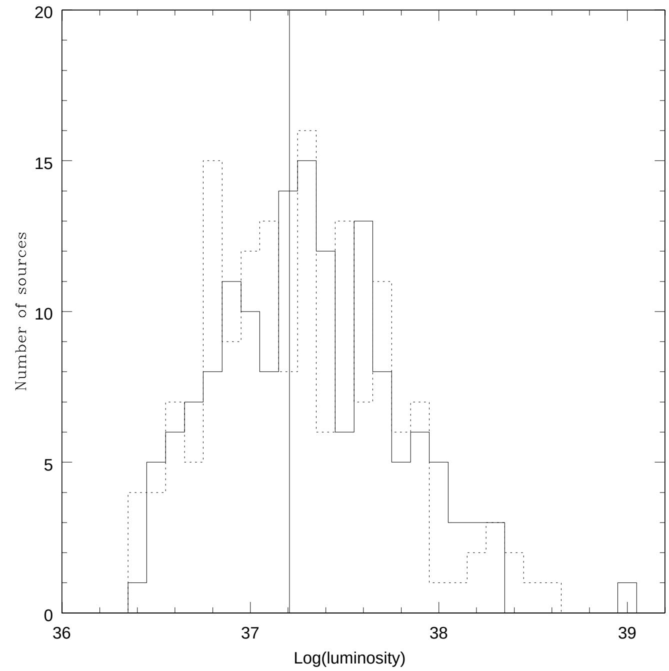


FIG. 6.—Differential luminosity functions of the two observations of Centaurus A in the 0.4–10 keV bandpass. The solid histogram is the first observation (OBSID 00316), and the dashed histogram is the second (OBSID 00962). The vertical line is the luminosity limit at which our sample is complete and unbiased. It is at the same flux as the vertical line in Fig. 5.

(Eskridge, Fabbiano, & Kim 1995a, 1995b, 1995c). Before *Chandra*, M31 was the only other relatively massive galaxy whose X-ray point source population had been well studied (Trinchieri & Fabbiano 1991; Primini, Forman, & Jones 1993; Supper et al. 1997). More recently, the X-ray point

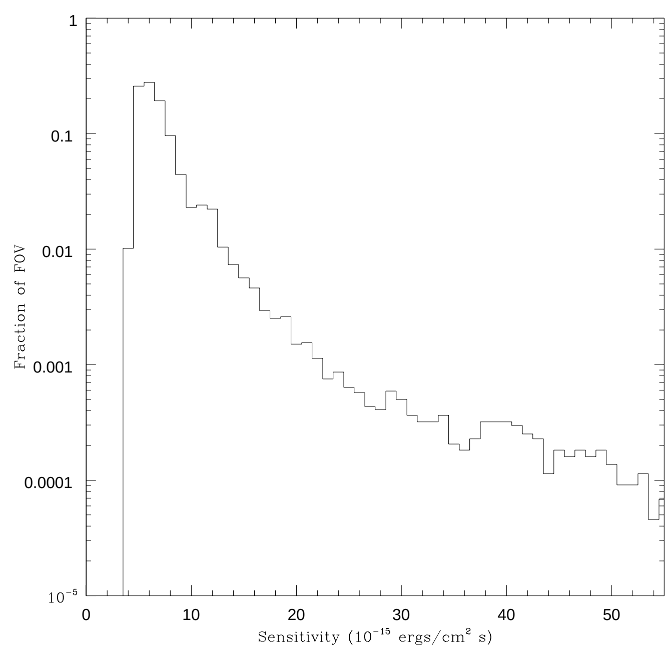


FIG. 7.—Fraction of the total solid angle vs. sensitivity in the 0.4–10 keV bandpass for the first (OBSID 00316) observation of Centaurus A in the 0.4–10 keV bandpass. The sensitivity of the second observation is similar. See text for details of this computation.

source population of the nearby elliptical galaxies M84 (Finoguenov & Jones 2001), NGC 4697 (Sarazin et al. 2000, hereafter SIB), NGC 1399, NGC 4472, and NGC 4636 (Lowenstein et al. 2000) have been observed with *Chandra*. These observations of the X-ray point source population of Cen A are therefore one of the few such studies of an elliptical galaxy, and only one of two (M84 being the other) of a galaxy with an active nucleus.

Figure 8 contains a plot of the luminosity function (LF) of all the X-ray sources in the Cen A field within 9′ (9 kpc) of the nucleus for each of the two observations (the black histograms). Only the sources within 9′ of the nucleus of

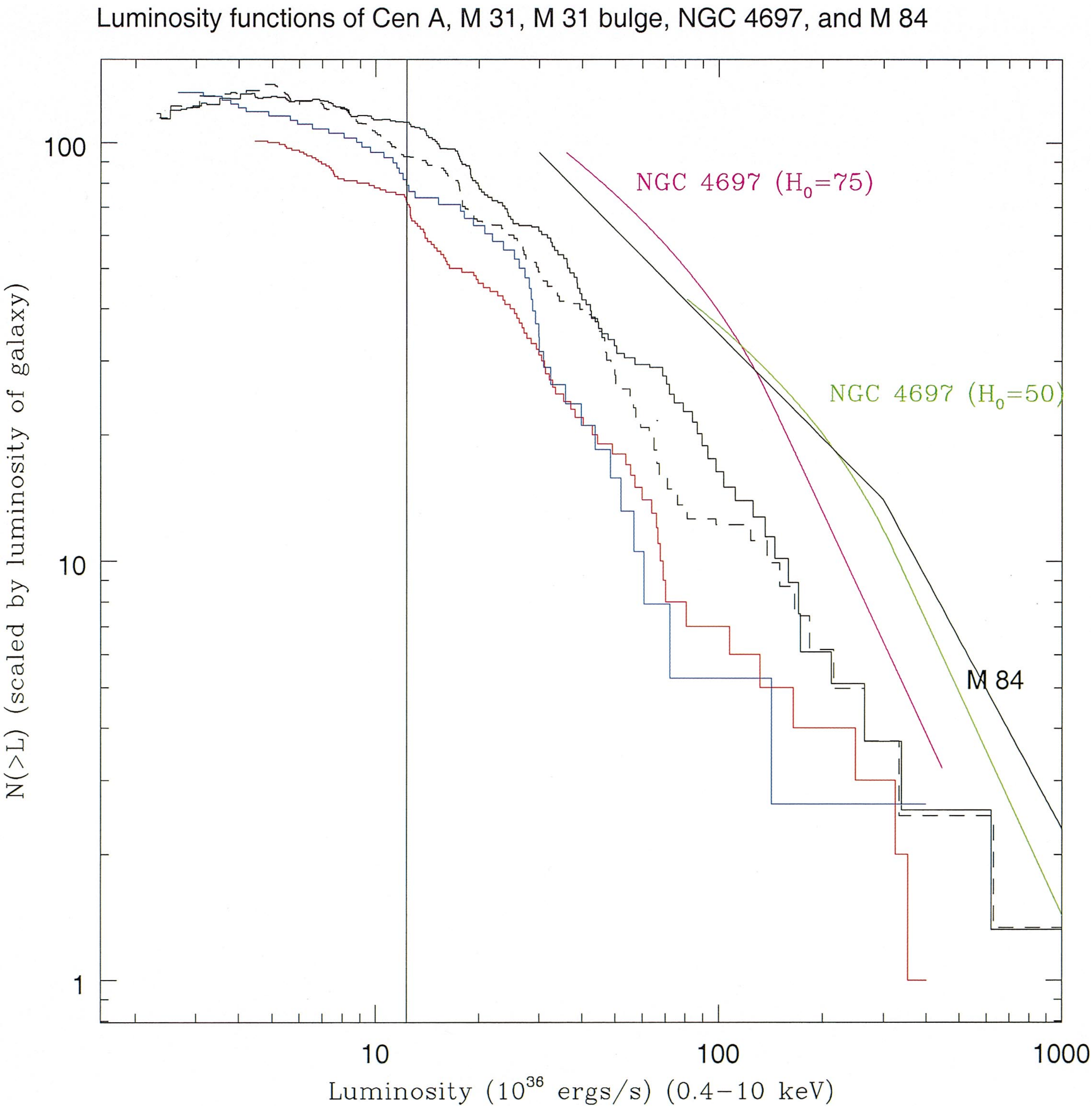


FIG. 8.—Luminosity functions of the X-ray point source populations in Cen A, M31, NGC 4697, and M84. The black histograms are the Cen A luminosity functions of all sources within 9′ of the nucleus of our first (*solid line*) and second (*dashed line*) observations, respectively, in the 0.4–10 keV bandpass with a correction for background AGNs removed. The red histogram is the LF of the sources of M31 from Trinchieri & Fabbiano (1991) and scaled to the 0.4–10 keV bandpass. The blue histogram is the LF of the sources in the bulge of M31 (within 7.′5 of the nucleus) taken from Primini et al. (1993) and scaled to the 0.4–10 keV bandpass. The LFs of the point sources in NGC 4697 (using $H_0 = 75$ km s$^{-1}$ Mpc$^{-1}$ and $H_0 = 50$ km s$^{-1}$ Mpc$^{-1}$) and M84 are plotted as continuous curves. All LFs have been scaled by the blue luminosity of the host galaxy.

Cen A were used as the majority of sources beyond this distance are probably unrelated foreground or background objects as described above. The Cen A LF has been corrected for background AGNs based on the log ($N$)–log ($S$) curve (see Fig. 5 determined for the *Chandra* Deep Field South (Giacconi et al. 2000). Also plotted are the LFs of all the sources in M31 (the red histogram) detected by the *Einstein* observatory (Trinchieri & Fabbiano 1991), the sources in the bulge of M31 (the blue histogram) taken from the *ROSAT* HRI observations (Primini et al. 1993), and *Chandra* observations of M84 (Finoguenov & Jones 2001) and NGC 4697 (SIB). These LFs have been normalized by the blue luminosity of the galaxy. A summary of the distances and luminosities of each of the galaxies is given in Table 3.

The blue luminosity weighted LFs of the X-ray point source population of Cen A is somewhat larger than that of the M31 bulge, and considerably larger than that of the entire galaxy. At a luminosity of $\sim 10^{37}$ ergs s$^{-1}$, there are about 10% more X-ray binaries per unit luminosity in Cen A than the M31 bulge, and about 25% more than in the whole of M31. The integrated X-ray luminosity of the XRBs in Cen A above a limiting luminosity of $10^{37}$ ergs s$^{-1}$ is $4.61 \times 10^{39}$ ergs s$^{-1}$. Both the qualitative similarity of the X-ray point source population of Cen A and the M31 bulge and the integrated X-ray luminosity of the XRBs in Cen A are consistent with the previously observed relationship between integrated X-ray luminosity and optical luminosity of elliptical and bulge-dominated spiral galaxies (Trinchieri et al. 2000; Matsumoto et al. 1997; Canizares, Fabbiano, & Trinchieri 1987).

At a luminosity of $\sim 10^{38}$ ergs s$^{-1}$, however, Cen A contains approximately twice the number of X-ray binaries per unit optical luminosity than either the M31 bulge or the whole of M31. While suggestive of differences in the XRB population between Cen A and M31, the statistical significance of this result is not large ($\sim 2\ \sigma$). In contrast, it appears that there are even larger populations of luminous X-ray binaries in NGC 4697 and M84, particularly above the Eddington limit for a 1.4 $M_\odot$ neutron star, compared with Cen A and M31. The LF of the X-ray point sources in NGC 4697 taken from SIB (their eq. [1]) is plotted as the green curve in Figure 8, and the LF of M84 taken from Finoguenov & Jones (2000) is shown as the continuous black curve.

This result relies somewhat on the assumed distance to the galaxies. Using the velocity relative to the CMB tabulated in Faber et al. (1989) and a value of $H_0 = 50$ km s$^{-1}$ Mpc$^{-1}$, SIB determine the distance to NGC 4697 be 15.9 Mpc. If one uses $H_0 = 75$ km s$^{-1}$ Mpc$^{-1}$ instead, the distance is 10.6 Mpc, and the corresponding luminosities of the X-ray sources are lower by a factor of 2.25. The blue luminosity of the galaxy is then reduced by the same factor. This would substantially reduce the number of super-Eddington sources in NGC 4697, but the number of "ordinary" luminous X-ray binaries per unit optical luminosity in NGC 4697, shown as the magenta curve in Figure 8, would still be considerably larger than either Cen A or the bulge of M31. We also investigated the effect of distance uncertainties (nominally 17 Mpc for M84) on the M84 LF, but we find that there is no plausible distance that would make the M84 luminosity function consistent with the others. A much larger region around M84 (20 kpc by 20 kpc) was used to create the luminosity function than was used for any of the other three galaxies. We speculate that perhaps there are a few bright halo sources (e.g., sources possibly related to distant globular clusters around M84) that were included in the M84 LF, and not in the LFs of the other galaxies. There are several hundred globular clusters around Cen A more than 20 kpc distant from the nucleus (Harris et al. 1984), so it is not implausible that a similar population exists for M84. If only a few of these around Cen A contained luminous X-ray binaries, the high-luminosity end of the LF could be significantly different. This would also support the claim of White (2000) that the LMXB population is directly related to the globular cluster population.

The optical emission from Cen A is, of course, partially obscured toward our line of sight by the dust lane that is thought to be the result of a merger with a spiral galaxy (Israel 1998). Since we are interested in comparing the LFs of the various galaxies by their relative starlight, it may be incorrect to weight the distributions by their blue light as the results could be distorted by variable extinction. To investigate this possibility, we have also compared the LFs of the four galaxies weighted by their $I$-band luminosities (Tully 1988; de Vaucouleurs et al. 1991; Tonry et al. 2001). The $B-V$ and $V-I$ colors of the three ellipticals are shown in Table 3. We find, however, that the relationship between LFs is unchanged if they are weighted by $I$-band luminosity instead of the $B$ band.

Based on spectral analysis of *ROSAT* and *ASCA* data, it has become apparent that there is a significant variance (as much as a factor of 4) in the relationship between X-ray flux of the LMXB component of the X-ray spectra of elliptical galaxies for a given optical (blue) luminosity (Trinchieri et al. 2000; White 2000). By resolving the individual sources in the galaxies, we directly confirm this variance. The reason for this large variation in number of XRBs per unit optical

TABLE 3

SUMMARY OF OPTICAL DATA AND DISTANCES TO GALAXIES WHOSE LUMINOSITY FUNCTIONS ARE PLOTTED IN FIG. 8

| Galaxy | $m_B$ | $d$ | $M_B$ | $L/L_{\rm M31}$ | $B-V$ | $V-I$ |
|---|---|---|---|---|---|---|
| M31 ............ | 3.56 | 690 kpc | −20.63 | 1 | | |
| M31 bulge ...... | 4.61 | 690 kpc | −19.58 | 0.38 | | |
| Cen A ........... | 7.48 | 3.5 Mpc | −20.24 | 0.70 | 1.00 | 1.078 |
| NGC 4697 ...... | 10.03 | 10.6 Mpc | −19.96 | 0.61 | 0.91 | 1.157 |
| M84 ............ | 10.18 | 17 Mpc | −20.97 | 1.37 | 0.98 | 1.191 |

NOTES.—The apparent blue magnitudes of M31, Cen A, and M84 were taken from Tully 1988. The apparent blue magnitude for NGC 4697 was taken from Faber et al. 1989. The colors for the elliptical galaxies were taken from de Vaucouleurs et al. 1991 and Tonry et al. 2001.

luminosity between the three ellipticals is unknown but is perhaps related to differences in the evolutionary star formation history of the galaxy (Wu 2001). White (2000) has argued that this variation is related to either the age of the host galaxy or variations in the globular cluster population. It will be interesting to compare these results with the results of future *Chandra* observations of other nearby elliptical galaxies to quantify the variation in the X-ray point source LF.

We have fitted a power law of the form $N(>L) = KL^{-\alpha}$ to the luminosity functions of Cen A to characterize the distribution and permit a quantitative comparison with the X-ray point source distribution in other galaxies. We restricted the lower limit to $10^{37}$ ergs s$^{-1}$ as below this value the statistical errors in our measurement of source luminosities become significant, and it is likely that below this limit we are missing sources because of statistical fluctuations. We find that fitting the distribution via nonlinear regression (not entirely appropriate as the data points are not independent), the maximum likelihood method of Crawford, Jauncey, & Murdoch (1970), and fitting the differential luminosity function (above a limiting luminosity of $3 \times 10^{37}$ ergs s$^{-1}$) give virtually identical results for the normalization and power-law index. We find a best-fit power-law index of $1.0 \pm 0.1$ for both observations. The one-sample Kolmogorov-Smirnov test indicates that this model is a statistically acceptable description of the distribution (Press et al. 1992). The uncertainty in the power-law index is derived using the variance of the maximum likelihood technique (Crawford et al. 1970). The luminosity functions for each observation with best-fit power-law models overlaid are shown in Figure 9.

A flattening of the luminosity function at roughly a luminosity of $2.5 \times 10^{37}$ ergs s$^{-1}$ was seen in the X-ray sources located in the bulge of M31 as observed with the *ROSAT* HRI (Primini et al. 1993) and has recently been confirmed by *XMM* observations (Shirey et al. 2001). The flattening of the M31 XRB LF and the consequent paucity of sources below this luminosity may be an indication of something fundamental in the formation and/or evolution of XRBs. As can be seen from Figure 9, there is clear evidence that the Cen A distribution is flattening below about $1.5 \times 10^{37}$ ergs s$^{-1}$. This flattening is statistically significant in the fit of the differential luminosity function if the fit is extended to a lower limit of $10^{37}$ ergs s$^{-1}$, but not in the maximum likelihood fitting technique (Crawford et al. 1970) as described above. As described in the previous paragraph, however, this is approximately the luminosity at which our source detections are becoming incomplete, so we cannot make a definitive statement as to whether this break seen in M31 is present in our Cen A data. A detailed Monte Carlo simulation is required to evaluate the statistical significance of this turnover, which is beyond the scope of this paper. This is also the flux where a significant fraction of the sources ($\sim 15\%$) are background AGNs, so the exact details of the background AGN luminosity function become important. A break in the LF around $3 \times 10^{38}$ ergs s$^{-1}$ (approximately the Eddington limit for a 1.4 $M_\odot$ star) was seen in recent *Chandra* observations of the elliptical galaxy NGC 4697 (SIB), but the number (three) of XRBs in Cen A above this luminosity is too small to make a meaningful comparison.

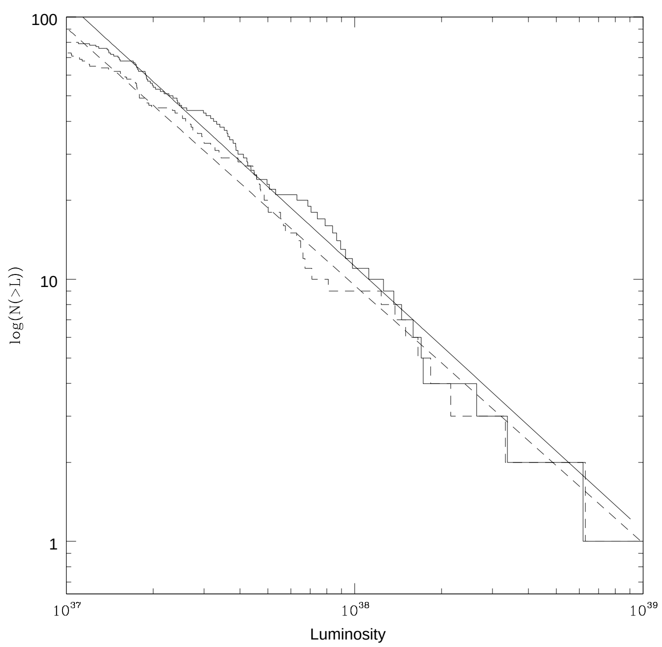


FIG. 9.—Luminosity function of the two Cen A observations (OBSID 00316—*solid line*; OBSID 00962—*dashed line*) with best-fit power law overlaid. An estimate of the contribution from background AGNs has been subtracted.

### 4.1. *Spectral Analysis*

To investigate trends in the spectral properties of all the sources, we created a "color-color" plot, shown in Figure 10. This diagram was created by binning the source spectra into three separate energy bins: $N1$ (number of counts between 0.4 and 1 keV—the soft band), $N2$ (1 to 2 keV—the intermediate band), and $N3$ (2 to 7 keV—the hard band). The two ratios $R1 = (N3 - N2)/(N1 + N2 + N3)$ and $R2 = (N2 - N1)/(N1 + N2 + N3)$ are plotted for each of the sources with 50 or more counts. The large square near the center of the plot represents our assumed 5 keV bremsstrahlung spectrum with galactic absorption column that was used in the luminosity calculation. The line that extends to the top of the plot from this point is the trail for a simulated 5 keV bremsstrahlung spectrum as the absorbing column is increased. The line that extends toward the bottom of the plot from this point represents simulated bremsstrahlung spectra with temperatures decreasing from 5 keV with constant (galactic) absorption. The model spectrum (5 keV bremsstrahlung with galactic absorption) that was used to convert the measured count rates to fluxes lies roughly in the middle of the distribution of sources in the color-color diagram, confirming that this spectrum is a reasonable description of the data. The hardest sources detected in our observation appear at the top of the plot. There are also two exceptionally soft X-ray sources detected in the second Cen A observation located at the far left of the diagram. We identify these as potential "super-soft" X-ray sources. One of these was within the FOV of both observations but only detected in one, implying considerable variability and possible transient behavior. These two "super-soft" sources have been labeled in Table 2.

### 4.2. *Temporal Variability*

Light curves were created for each of the sources to search for variability within a given observation. The source counts were binned into 10 equally spaced time bins ($\sim 3600$ s per bin), and the $\chi^2$ was computed for each light

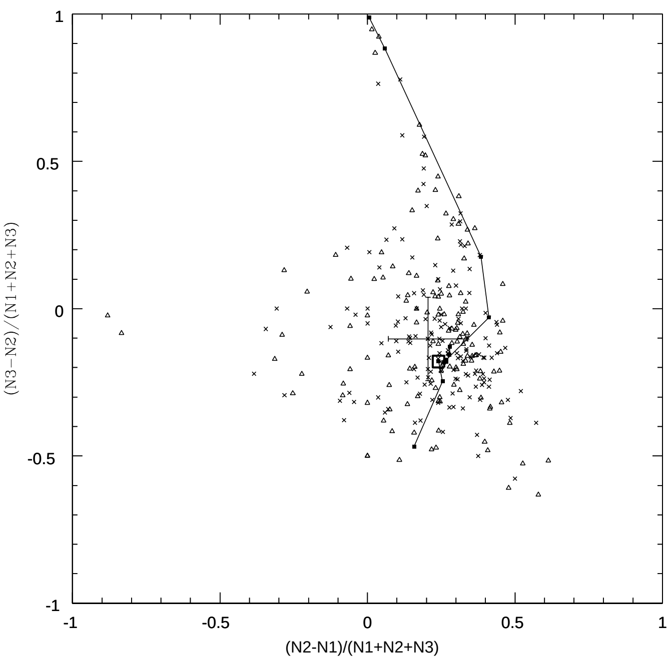


FIG. 10.—Color-color diagram of all the point sources in the Cen A observations. The source counts were binned into three bands, $N1$, $N2$, and $N3$, that correspond to the 0.4–1, 1–2, and 2–7 keV bands, respectively. The crosses represent the sources in the first (OBSID 00316) observation, and the triangles those of the second (OBSID 00962). The large square in the center is the position of a hypothetical source with a 5 keV bremsstrahlung spectrum and an absorbing column of $7 \times 10^{20}$ cm$^{-2}$. The line going up the plot from the box corresponds to a 5 keV spectrum with increasing absorption, the line going down to decreasing temperature with constant (galactic) absorbing column. A sample error bar for a 40 count source is shown.

curve against the hypothesis of no variability. Two sources showed significant short-term variability and are labeled in Table 2. One of these is discussed in more detail below. We also performed an FFT on the event list of each source to search for more rapid, regular variation (e.g., pulsations) that the light curve analysis would not have detected. There were no statistically significant detections of any regular periodicities.

In addition to searching for short-term variability within a given observation, we compared the luminosities of the sources between the two observations to search for long-term variability. For the sources that were within the overlapping region of the FOV in the two observations (about $\frac{1}{4}$ of the FOV of each of the observations) and that were detected in both, we identified a source as variable if the exposure corrected luminosity varied by more than 3 $\sigma$. Of the 82 sources that were detected in both observations, eight met this criterion. Thirty-eight other sources within this overlapping region were only detected in one of the two observations. A 3 $\sigma$ fluctuation in the background rate at the location of a given source was used to place an upper limit on the source luminosity. If the measured luminosity of the source in the observation in which it was detected was greater than this upper limit in the observation in which it was not detected, the source was identified as variable. Twenty-seven of the 38 sources met this criterion for variability. We therefore find that a total of 35 (8 + 27) of the 246 sources exhibit long-term variability. These sources are labeled with "ltv" in the NOTES column of Table 2. Note that this is probably an overestimate of the number of variable sources in our observation for two reasons. First, several of the sources that we have labeled as variable have a luminosity just above the upper limit in the other observation. A small change in our upper limit (say to 4 $\sigma$) would remove them from this group. Second, some of the sources are located in the gap between chips or at the edge of the field of view where the uncertainty in the exposure correction is large.

## 5. INDIVIDUAL SOURCES

In this section, we discuss individual sources based on their spectra and/or light curves.

### 5.1. *CXOU J132507.5−430410*

This is one of the brightest sources in the field and is located near the edge of the SW radio lobe. It has been previously detected by *Einstein* (Feigelson et al. 1981) and *ROSAT* (Wagner, Döbereiner, & Junkes 1996; Turner et al. 1997). This object was suggested to be either a 14th magnitude foreground M star (Feigelson et al. 1981) or a background active galaxy (Wagner et al. 1996). This source corresponds to a bright optical source in the DSS image. For these reasons, we identify this object as a foreground star. The flux from this source increased by a factor of 2 between the first and second observations. If this source is located within Cen A, it would be a super-Eddington source with an X-ray luminosity of $\sim 10^{39}$ ergs s$^{-1}$ in the second observation. During this second observation the source flared with the X-ray flux increasing by more than an order of magnitude in less than 2000 s (see Fig. 11). Such rapid variability strongly argues against this object being a background galaxy. If it is within our galaxy ($d = 10$ kpc), its luminosity ($\sim 10^{34}$ ergs s$^{-1}$) is below that of typical accreting neutron stars, but above that of cataclysmic variables. Our data strengthen the suggestion of Feigelson et al. (1981)

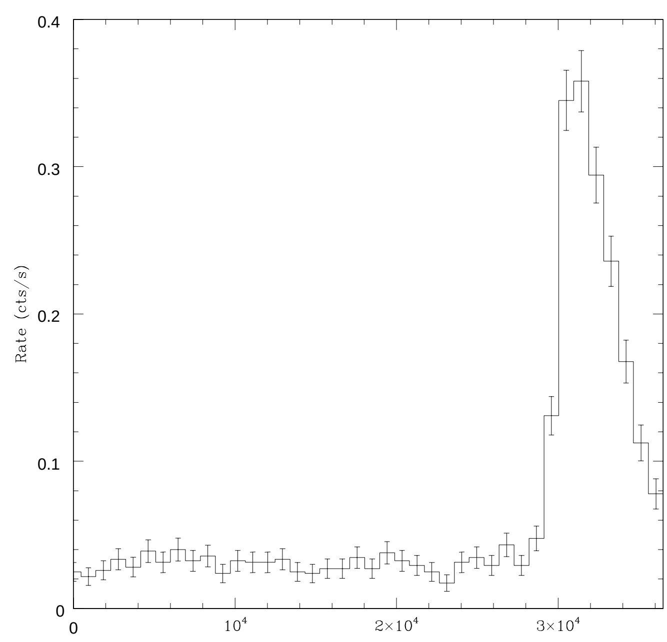


FIG. 11.—Light curve of source CXOU 132507.5−430410 during second (OBSID 00962) observation. The data are divided into 925 s time bins.

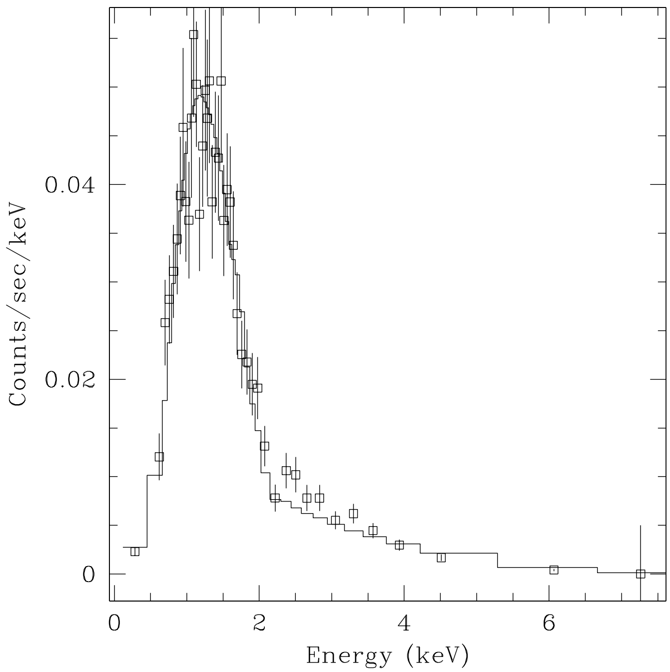


FIG. 12.—Spectrum and best-fit absorbed power-law model (photon index = $2.48 \pm 0.12$ and $N_H = 3.44 \pm 0.5 \times 10^{21}$ cm$^{-2}$) of source CXOU J132520.0−430317, a possible super-Eddington transient.

that this object is a foreground M dwarf. The rapid time variability of this object indicates that it may be a flare star. It has not been included in the luminosity function described above.

### 5.2. *CXOU J132526.4−430054*

This source is located approximately 20″ to the NW of the nucleus in the dust lane of the galaxy. This source was singled out because it is bright and has a very hard spectrum. It is located at the top of the color-color diagram (see Fig. 10). Fitting the spectrum with an absorbed power law, we find a spectral (photon) index of $0.94 \pm 0.20$ and an absorbing column of $1.5 \pm 0.5 \times 10^{22}$ cm$^{-2}$ with a flux of $2.69 \times 10^{-13}$ ergs cm$^{-2}$ s$^{-1}$. Its location in the dust lane may produce the large column. The luminosity in Table 2 is an underestimate as the spectrum is much harder than assumed. Using the best-fit spectrum, the luminosity in the 0.4–10 keV bandpass is $4.3 \times 10^{38}$ ergs s$^{-1}$. No significant variability was seen between the two observations. Whether this is an XRB within Cen A or a background AGN is unclear, but such a hard spectrum is not typical of either X-ray bright AGNs or LMXBs. It is possible, however, that this object is a HMXB system within the dust lane of the galaxy, for which the hard spectrum and large column density would not be considered unusual (Lewin et al. 1994).

### 5.3. *CXOU J132519.9−430317*

This bright, recurrent X-ray transient, located about 2.′5 to the SW of the nucleus, was first detected in *ROSAT* HRI observations of Cen A (Steinle, Dennerl, & Englehauser 2000). The luminosity, assuming the source is located in Cen A, was $\sim 3 \times 10^{39}$ ergs s$^{-1}$ in the 0.1–2.4 keV *ROSAT* band. We detected this bright transient in the first of our *Chandra* observations, but not in the second. The source spectrum and best-fit absorbed power-law model are shown in Figure 12. The spectrum is well fitted by a power law with photon index $2.48 \pm 0.12$ and $N_H = 3.44 \pm 0.5 \times 10^{21}$ cm$^{-2}$ (the uncertainties are the 90% confidence intervals). The flux is $5.64 \times 10^{-13}$ ergs cm$^{-2}$ s$^{-1}$ in the 0.4–10 keV bandpass. If this object is located in Cen A, its *Chandra* luminosity in the 0.4–10 keV bandpass would be $1.57 \times 10^{39}$ ergs s$^{-1}$, placing this source above the Eddington limit for conventional X-ray binaries. Detections of such super-Eddington sources are becoming commonplace in observations of other galaxies (Makishima et al. 2000; Fabbiano et al. 2000), and the properties of this source are not inconsistent with those other sources. The upper limit (3 $\sigma$—as computed above in § 4.2) to the source luminosity in the second observation is $2.94 \times 10^{36}$ ergs s$^{-1}$, a decrease in luminosity by more than a factor of 500. Such large variability strongly argues against this object being a background galaxy.

## 6. SUMMARY AND CONCLUSIONS

We detected 246 X-ray sources in the vicinity of Cen A in two 36 ks *Chandra* ACIS-I observations above a luminosity limit of $\sim 2.2 \times 10^{36}$ ergs s$^{-1}$ in the 0.4–10 keV bandpass. Our sample is complete and unbiased above a luminosity of $\sim 1.3 \times 10^{37}$ ergs s$^{-1}$. Of these 246 sources, 120 were within the field of view of both observations, but only 82 were actually detected in both. Two sources showed significant variability during an observation, and 35 others exhibited statistically significant variability between the two observations. The radial distribution of sources is centrally peaked at the nucleus of the galaxy and approaches a constant value ($\sim$0.25 sources per arcmin$^2$) consistent with background AGNs approximately 9′ from the nucleus which is roughly the optical ($D_{25}$) size of the galaxy. We find nine sources coincident with globular clusters around Cen A. All of the sources detected by the *ROSAT* HRI and PSPC instruments that were within our field of view have been detected. An X-ray flare was detected in one source that is probably a foreground object, and the previously known super-Eddington transient in Cen A was detected in one observation.

We found that the luminosity function of the point sources within Cen A is similar to that of the M31 bulge, but the number of XRBs per unit blue luminosity in Cen A is greater than M31 as a whole. The luminosity functions of two other elliptical galaxies observed with *Chandra*, NGC 4697 and M84, imply a considerably larger number of luminous X-ray binaries per unit blue luminosity than either Cen A or M31. The reason for this is unknown but could be related to differences in the early history of the galaxies. We await the results of *Chandra* observations of other elliptical galaxies to address the question of the variation of the XRB population with blue luminosity in greater detail.

This work was supported by NASA contracts NAS8-38248 and NAS8-39073, the *Chandra* Science Center, and the Smithsonian Institution. J. M. K. was supported by the REU Intern Program funded by the National Science Foundation. The Digitized Sky Survey was produced at the Space Telescope Science Institute under US Government grant NAG W-2166. We would like to thank Gregory Bothun and the anonymous referee for a critical reading of this paper and suggestions. We would also like to thank Paul Voytas for computer support.

REFERENCES

Aldcroft, T. A., Karovska, M., Cresitello-Dittmar, M. L., Cameron, R. A., & Markevitch, M. L. 2000, Proc. SPIE, 4012, 650
Blanton, E. L., Sarazin, C. L., & Irwin, J. A. 2001, ApJ, 552, 106
Burns, J. O., Feigelson, E. D., & Schreier, E. J. 1983, ApJ, 273, 128
Canizares, C. R., Fabbiano, G., & Trinchieri, G. 1987, ApJ, 312, 503
Clarke, D. A., Burns, J. O., & Norman, M. L. 1992, ApJ, 395, 444
Crawford, D. F., Jauncey, D. L., & Murdoch, H. S. 1970, ApJ, 162, 405
de Vaucouleurs, G., de Vaucouleurs, A., Corwin, H. G. Jr., Buta, R. J., Paturel, G., & Fouqué, P. 1991, Third Reference Catalog of Bright Galaxies (New York: Springer)
Eskridge, P. B., Fabbiano, G., & Kim, D.-W. 1995a, ApJS, 97, 141
———. 1995b, ApJ, 442, 523
———. 1995c, ApJ, 448, 70
Fabbiano, G., Kim, D.-W., & Trinchieri, G. 1994, ApJ, 429, 94
Fabbiano, G., Zezas, A., & Murray, S. S. 2000, ApJ, 554, 1035
Faber, S. M., Wegner, G., Burstein, D., Davies, R. L., Dressler, A., Lynden-Bell, D., & Terlevich, R. J. 1989, ApJS, 69, 763
Feigelson, E. D., Schreier, E. J., Delvaille, J. P., Giacconi, R., Grindlay, J. E., & Lightman, A. P. 1981, ApJ, 251, 31
Finoguenov, A., & Jones, C. 2001, ApJ, 547, L107
Giacconi, R., et al. 2000, preprint (astro-ph/0007240)
Harris, G. L., Geisler, D., Harris, H. C., & Hesser, J. E. 1992, AJ, 104, 613
Harris, G. L. H., Hesser, J. E., Harris, H. C., & Curry, P. J. 1984, ApJ, 287, 175
Irwin, J. A., Bregman, J. N., & Sarazin, C. L. 2000, BAAS, 197, 111.14
Irwin, J. A., & Sarazin, C. L. 1998, ApJ, 499, 650
Israel, F. P. 1998, A&A Rev., 8, 237
Karovska, M., et al. 2000, in IAU Symp. 205, Galaxies and Their Constituents at the Highest Angular Resolution, ed. R. T. Schilizzi, S. Vogel, F. Paresce, & M. Elvis (San Francisco: ASP), 45
Kraft, R. P., et al. 2000, ApJ, 531, L9
Kraft, R. P., et al. 2001, ApJ, submitted
Lewin, W. H. G., van Paradijs, J., & van den Heuvel, E. P. J. 1994, X-ray Binaries (Cambridge: Cambridge Univ. Press)
Lowenstein, M., Angelini, L., Mushotzky, R. F., & Arnaud, K. A. 2000, AAS Head Meeting, 31, 15.01
Makishima, K., et al. 2000, ApJ, 535, 632
Matsumoto, H., et al. 1997, ApJ, 482, 133
Matsumoto, H., et al. 2001, ApJ, 547, L25
Minitti, D., et al. 1996, ApJ, 467, 221
Monet, D. 1998, BAAS, 193 120.03
Primini, R. A., Forman, W., & Jones, C. 1993, ApJ, 410, 615
Press, W. H., Teukolsky, S. A., Vetterling, W. T., & Flannery, B. P. 1992, Numerical Recipes in C (Cambridge: Cambridge Univ. Press)
Sarazin, C. L., Irwin, J. A., & Bregman, J. N. 2000, ApJ, 544, L101
Schiminovich, D., van Gorkom, J. H., van der Hulst, J. M., & Kasow, S. 1994, ApJ, 423, L101
Shirey, R., et al. 2001, A&A, 365, L195
Steinle, H., Dennerl, K., & Englhauser, J. 2000, A&A, 375, L57
Supper, R., et al. 1997, A&A, 317, 328
Tennant, A. F., Wu, K., Ghosh, K. K., Kolodziejczak, J. J., & Swartz, D. A. 2001, ApJ, 549, L43
Tingay, S. J., et al. 1998, AJ, 115, 960
Tonry, J. L., et al. 2001, ApJ, 546, 681
Trinchieri, G., & Fabbiano, G. 1985, ApJ, 296, 447
———. 1991, ApJ, 382, 82
Trinchieri, G., et al. 2000, A&A, 364, 53
Tully, R. B. 1988, Nearby Galaxy Catalog (Cambridge: Cambridge Univ. Press)
Turner, T. J., George, I. M., Mushotzky, R. F., & Nandra, K. 1997, ApJ, 475, 118
Wagner, S. J., Döbereiner, S., & Junkes, N. 1996, in Proc. Röntgenstrahlung from the Universe, ed. H. U. Zimmermann, J. Trümper, & H. Yorke (MPE Rep. 263), 521
Weisskopf, M. C., Tananbaum, H. D., Van Speybroeck, L. P., & O'Dell, S. L. 2000, Proc. SPIE, 4012, 2
White, R. 2000, American Astronomical Society, HEAD meeting 32, 15.12
Wu, K. 2001, ApJ, in press (astro-ph/0103157)